nature communications

Article

https://doi.org/10.1038/s41467-026-69875-2

CO_2 radiative forcing induces summer cooling over India

Received: 6 November 2025

Accepted: 12 February 2026

Published online: 24 March 2026

Check for updates

Jinhong Liu[1,2], Xia Qu[1] ✉, Gang Huang[2,3] ✉ & Chenglin Lyu[2,3]

In response to anthropogenic forcing, the Earth's surface generally warms as greenhouse gases trap outgoing longwave radiation. Counterintuitively, however, some regions exhibit surface cooling against this global warming background—a phenomenon known as a warming hole. Beyond the well-documented warming holes over the North Atlantic and southeastern United States, here we show that increasing atmospheric CO_2 concentrations can also induce summertime cooling over India. Due to the direct radiative effect of CO_2, warming of the Eurasian continent relative to surrounding oceans, low-level moisture transport and vertical motion are enhanced over India. Combined with abundant summer-monsoon moisture and the topographic blocking effects of the Himalayas and Hindu Kush Mountains, these circulation changes increase cloud cover. The resulting cloud enhancement reduces incoming solar radiation at the surface, producing the observed regional cooling. These results reveal a previously underappreciated mechanism whereby greenhouse gas forcing can paradoxically induce regional cooling through atmospheric dynamical pathways.

Since the onset of the Industrial Revolution, global warming has emerged as the most prominent feature of climate change. The Sixth Assessment Report of the Intergovernmental Panel on Climate Change (IPCC AR6) confirms that the last four decades have each been successively warmer than any decade since 1850[1]; the global mean surface temperature in 2024 increased by about 1.5 °C compared to pre-industrial levels[2,3]. A large body of observational evidence and model simulations consistently indicates that anthropogenic greenhouse gas emissions are the dominant driver of this warming[1]. However, regional manifestations of climate change are far from uniform, with considerable heterogeneity in both the magnitude and pattern of temperature responses[4,5]. Regional variations are particularly critical, as they determine local impacts on ecosystems, agriculture, and human health[6,7]. Against this backdrop, some regions have exhibited significantly weaker warming, or even surface cooling, during the global warming era—a counterintuitive phenomenon commonly referred to as the "warming hole"[8–10].

The warming hole has been robustly identified in two well-studied regions: the subpolar North Atlantic and the southeastern United States. In the North Atlantic, the muted warming signal is strongly linked to ocean dynamics, particularly the weakening of the Atlantic Meridional Overturning Circulation, greenhouse gas–induced changes in ocean heat transport, reductions in anthropogenic aerosols, and associated atmosphere–ocean interactions[9,11–16]. In contrast, the southeastern United States warming hole has been attributed to a combination of factors including internal climate variability, aerosol forcing, and radiative forcing–induced sea surface temperature anomalies[10,17–21]. Together, these studies demonstrate that warming holes may arise from a range of mechanisms that vary across regions, but most explanations emphasize the central role of ocean circulation changes or aerosol forcing.

Recently, a warming hole feature over India was found by scientists[22]. As a monsoon-dominated region spanning tropical and subtropical latitudes, with a dense population and an economy heavily dependent on agriculture, India is highly vulnerable to temperature changes. The impacts of extreme heat events in recent years underscore this vulnerability: a devastating coastal heatwave in 2015 claimed

[1]Center for Monsoon System Research, Institute of Atmospheric Physics, Chinese Academy of Sciences, Beijing, China. [2]University of Chinese Academy of Sciences, Beijing, China. [3]State Key Laboratory of Earth System Numerical Modeling and Application, Institute of Atmospheric Physics, Chinese Academy of Sciences, Beijing, China. ✉e-mail: quxia@mail.iap.ac.cn; hg@mail.iap.ac.cn

around 2500 lives[23]; the extreme March 2022 heatwave pushed temperatures above 40 °C in numerous Indian cities[24]; and in 2024 India recorded both its highest observed temperature and its longest continuous spell of heatwave[25]. These extreme heat events are closely linked to North Atlantic sea surface temperature anomalies, warming of the tropical Indian Ocean, El Niño events, and local land–atmosphere feedbacks[26–28]. Despite the increasing frequency and severity of such extreme heat events, long-term surface temperature trends over India feature a warming hole, with in-situ warming roughly half of the global average[22]. Existing hypotheses point to anthropogenic aerosols, changes in large-scale circulation, and irrigation expansion as possible drivers of this muted warming signal. However, these explanations remain debated.

Here, using multi-model ensembles of both atmosphere-only and atmosphere-ocean coupled simulations, we present evidence for a previously underappreciated mechanism: CO_2 forcing itself, in the absence of ocean-associated processes, can induce a summer cooling over India (Fig. 1). This finding differs from the prevailing view that regional warming holes are necessarily tied to ocean circulation changes or aerosol forcing. Instead, it highlights the capacity of direct radiative forcing from greenhouse gases to reshape atmospheric circulation and alter the land–atmosphere energy balance in ways that produce localized cooling.

Results

CO_2-induced summer cooling over India

During boreal summer, even without ocean-related processes, CO_2 radiative forcing induces a distinct surface cooling over India. To assess its robustness, we analyzed two experiment sets from Coupled Model Intercomparison Project phase six (CMIP6): amip-related simulations (amip and amip-4 × CO_2 simulations) and the abrupt-related simulations (abrupt-4 × CO_2 and piControl simulations), hereafter referred to as "amip" results and "abrupt" results, respectively. Details of the method used to isolate the effects of CO_2 radiative forcing are provided in Methods (see "Methods": Quantification of CO_2 radiative forcing effects). Twelve models participated in amip-related simulations and 48 in abrupt-related simulations.

Figure 1 demonstrates the response of surface air temperature to CO_2 radiative forcing during local summer. When the sea surface temperature is fixed to its present-climate level and atmospheric CO_2 concentration is quadrupled, most land areas exhibit strong warming in amip-related results (Fig. 1a). The global mean surface air temperature increases by 0.91–2.15 K, with enhanced warming over mid-latitude Eurasia and North America, reaching a maximum of 3.48 K in the multi-model ensemble (MME). Given the smaller number of models participating in amip-related results, we also examine the abrupt-related results (Fig. 1d, e), which display a similar pattern but a stronger amplitude, with global mean warming of 0.85–2.56 K and MME maximum up to 5.49 K over the center region of the United States.

In contrast, both ensembles reveal a robust summer cooling over India in response to CO_2 radiative forcing alone. When the CO_2 concentration is quadrupled, and the sea surface temperature is fixed, cooling occurs south of the Himalayas and the Sulaiman Range (Fig. 1b). The maximum cooling ranges from −2.55 to −0.68 K across the models. The abrupt-related results display comparable patterns (Fig. 1e), with maximum cooling ranging from −9.93 to −0.20 K across

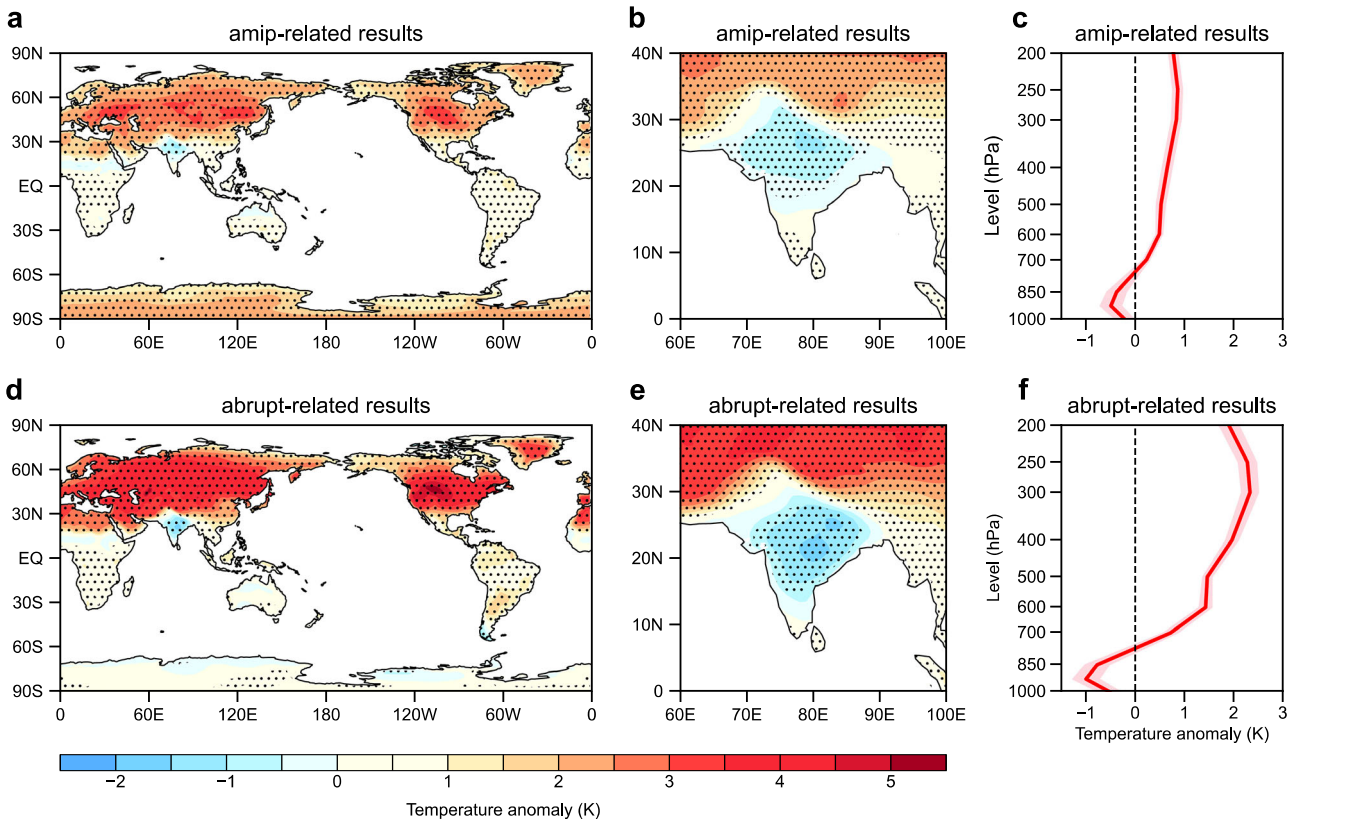

Fig. 1 | Surface air temperature responses to CO_2 radiative forcing. a The response of surface air temperature over the global land regions during local summer for the AMIP-related results. **b** Same as (**a**), but focusing on the Indian subcontinent. The responses are the multi-model ensemble (MME) results. The black dots indicate regions where at least 75% of models agree on the sign of the MME. **c** The vertical profile of the area-averaged air temperature response (red line) over the Indian domain [15–28 °N, 72–87 °E] for the amip-related results. Pink shadings indicate the 95% confidence intervals of the multi-model ensemble (MME). These are calculated based on $\pm 1.96 \times \sigma/\sqrt{N}$, where σ denotes the standard deviation across the models, and N is the number of models. **d**–**f** Same as (**a**–**c**), but for the abrupt-related results. The units are K.

the models. Furthermore, the results for the same set of "amip" and "abrupt" models indicate that the spatial pattern is consistent with that in Fig. 1, showing robust warming over the mid-latitude Eurasia and North America, along with a distinct surface summer cooling response over the Indian region (Supplementary Fig. 1).

The summer cooling could have contributed to a cooling of more than 0.1 K since 1950. Here, we assume that: (1) the relation between radiative forcing and CO_2 concentration is logarithmic; and (2) the radiative forcing-temperature relationship is linear. Using the annual mean of CO_2 concentration in 2024 (422.80 ppm)[29], the summer cooling in amip-related results corresponds to 0.17 K relative to the pre-industrial level (284.70 ppm) and 0.11 K relative to 1950 (312.0 ppm)[30]. The corresponding values in abrupt-related results are 0.29 K and 0.23 K, respectively.

This cooling signal is vertically confined to the lower troposphere. Area-averaged profiles over the Indian domain [15–28 °N, 72–87 °E] indicate that cooling occurs mainly below 850 hPa, transitioning to warming aloft (Fig. 1c, f, Supplementary Fig. 2).

Seasonally, the cooling is limited to June–August, coinciding with the Indian summer monsoon (Fig. 2, Supplementary Fig. 3). In September, the model results diverge, and during the rest of the year, India experiences surface warming in response to increased CO_2 concentration.

Changes in surface energy fluxes and their drivers

A surface energy budget analysis provides insights into the cooling over India. The reduction in downward solar radiation is the dominant contributor to the surface cooling. Figure 3 displays the response of surface energy fluxes over India, where both the amip-related and abrupt-related results consistently indicate that reduced solar radiation drives the cooling. This decline in downward solar radiation is further linked to enhanced cloud cover (color shadings in Fig. 4a, d).

The cloud increase is primarily caused by strengthened atmospheric ascent (contours in Fig. 4a, d). When CO_2 concentration rises, and the sea surface temperature is fixed, the Eurasia continent warms (Fig. 1), intensifying the lower-tropospheric southwesterlies toward India (vectors in Fig. 4b, e). The topographic barrier of the Himalayas and the Hindu Kush, together with abundant monsoonal moisture (Fig. 4c, f), favors strong ascent-precipitation feedback, further amplifying vertical motion over India.

Enhanced moisture transport also reinforces cloud formation. The greater continental warming relative to the Indian Ocean strengthens the land-sea thermal contrast, increasing the moisture flux into India (Fig. 4b, e) and promoting local cloud development.

Furthermore, the amip-related results indicate that increased CO_2 leads to pronounced warming in the upper troposphere, resulting in a more stable troposphere[31]. This enhanced stability suppresses con-

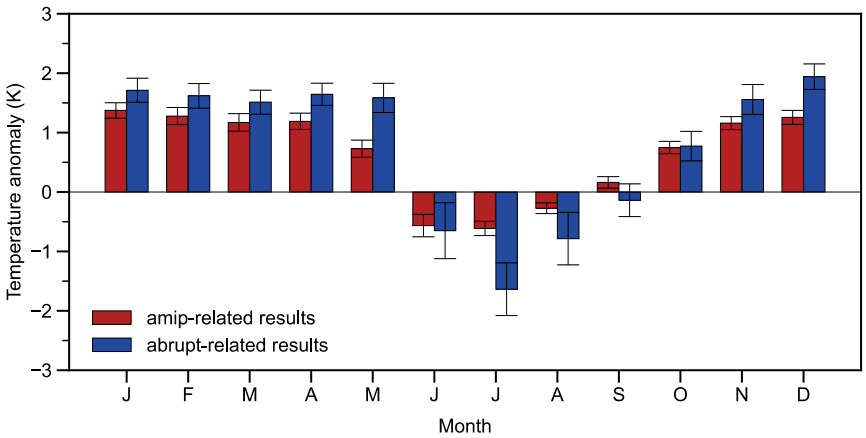

Fig. 2 | Monthly surface air temperature response over India. Area-averaged surface air temperature responses for each calendar month over the Indian domain [15–28 °N, 72–87 °E]. The red and blue bars indicate the amip-related and abrupt-related results, respectively. Error bars denote the 95% confidence intervals of the multi-model ensemble (MME). These are calculated based on $\pm 1.96 \times \sigma/\sqrt{N}$, where σ denotes the standard deviation across the models, and N is the number of models. The units are K.

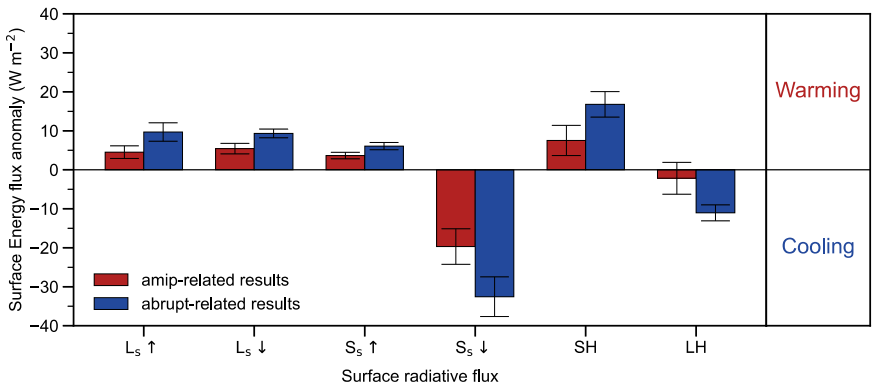

Fig. 3 | Surface energy fluxes responses over India. L and S are the longwave and solar radiative fluxes, respectively. The subscript "s" denotes the surface. The arrows (↑ and ↓) in superscript represent the direction of radiative fluxes. SH and LH are the sensible and latent fluxes. The red and blue bars correspond to the amip-related and abrupt-related results, respectively. Positive means the flux change favors surface warming; negative means the flux change favors surface cooling. Error bars denote the 95% confidence intervals of the multi-model ensemble (MME). These are calculated based on $\pm 1.96 \times \sigma/\sqrt{N}$, where σ denotes the standard deviation across the models, and N is the number of models. The units are W m^{-2}.

https://doi.org/10.1038/s41467-026-69875-2

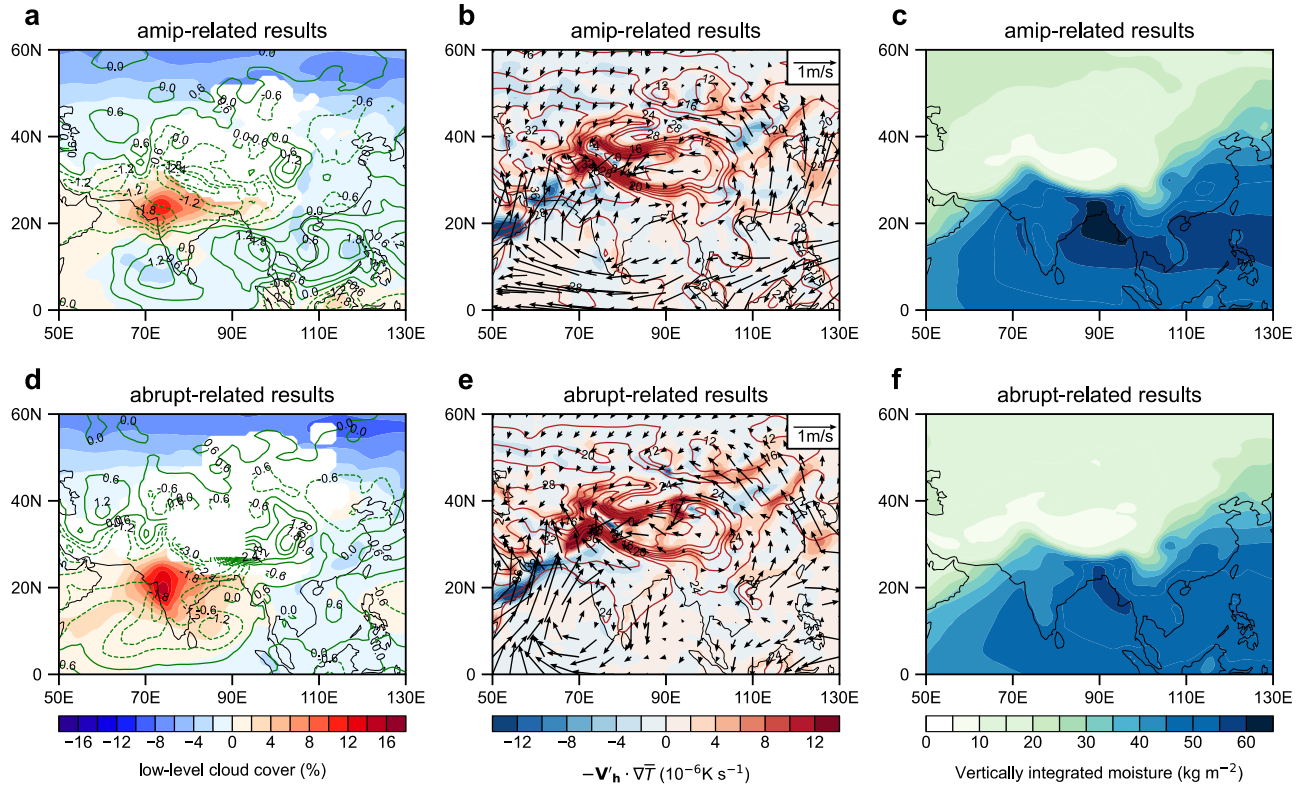

Fig. 4 | The responses, climatology of some climate elements and the associated horizontal temperature advection. a Response of low-level cloud cover (shadings; unit: %) and pressure velocity at 500 hPa (contours; unit: 10^{-2} Pa s^{-1}) for the amip-related results. **b** Response of climatological temperature advection by anomalous horizontal wind (shadings; unit: 10^{-6} K s^{-1}), near-surface wind (vectors; unit: m s^{-1}) and the climatological near-surface air temperature (color lines; unit: °C) for the amip-related results. **c** Climatology of vertically integrated specific humidity from the surface to 1 hPa (unit: kg m^{-2}) for the amip simulations **d**–**f** Same as (**a**–**c**), but for the abrupt-related results. For the climatology, 1979–2008 are used for the amip simulations, and the last 100 years are used for the piControl simulations.

vection over the southeastern Arabian Sea, the Bay of Bengal, and the South China Sea (Fig. 4a). The weakened tropical convection promotes anomalous moisture convergence toward the Indian subcontinent, thereby favoring cloud development. Notably, such a convective suppression–moisture convergence mechanism is absent in the abrupt-related results (Fig. 4d), probably due to the existence of air-sea interaction.

Among the surface thermodynamics terms, latent heating exhibits a weak cooling tendency but is statistically insignificant in AMIP-related results. The surface cooling reduces the temperature gap between the ground and overlying air, thereby diminishing surface latent heating release. This implies that the changes in surface latent heating are a consequence, rather than a cause, of the surface cooling.

Taken together, the CO_2-induced enhancement of ascent and moisture transport leads to increased cloud cover and reduced solar heating over India. Similar behavior is found in models of the Coupled Model Intercomparison Project phase 5 as well (ref. 32).

Contributions of near-surface air processes

The thermodynamic budget of near-surface air at 2 m is mainly governed by horizontal advection and adiabatic heating (See "Methods": Thermodynamic framework for near-surface air temperature at 2 m). The adiabatic term includes sensible and latent heating captured by near-surface air, making its direct evaluation difficult. Figure 5 displays the horizontal temperature advection components. When the sea surface temperature is fixed, the enhanced southwesterlies following the increase in CO_2 concentration transport relatively cool air from the Arabian Sea into inland India, producing cold advection (Fig. 4b, e). Area-averaged results over [15–28 °N, 72–87 °E] show that the contribution of climatological temperature advected by anomalous horizontal wind ($-\boldsymbol{V_h}'\cdot\nabla\overline{T}$) is insignificant in amip-related results but significant in abrupt-related results (Fig. 5). In contrast, the anomalous temperature transported by climatological horizontal wind ($-\overline{\boldsymbol{V_h}}\cdot\nabla T'$) produces a warming tendency, partially offsetting the cold advection (Fig. 5). The residual terms, inferred from the addition of $-\boldsymbol{V_h}'\cdot\nabla\overline{T}$ and $-\overline{\boldsymbol{V_h}}\cdot\nabla T'$, are small in amip-related results but become comparable to, or even exceed $-\boldsymbol{V_h}'\cdot\nabla\overline{T}$ in abrupt-related simulations.

This near-surface cooling is also modulated by surface processes. In response to the increase in CO_2 concentration alone, changes in surface sensible heating tend to favor local warming (Fig. 3). This suggests that near-surface cooling does not directly benefit surface cooling. Instead, in addition to the cold advection led by surface wind change, the surface cooling further contributes to lowering the near-surface air temperature.

Seasonal dependence of the cooling

The occurrence of CO_2-induced surface cooling over India exhibits a clear seasonal dependence, confined primarily to the boreal summer. This behavior is closely linked to variations in ambient moisture. Figure 6 demonstrates the annual cycle of column precipitable water averaged over [15–28 °N, 72–87 °E]. From June to September, the precipitable water levels are higher than those in other months, providing a favorable environment for enhanced convection and the occurrence of ascent-precipitation-cloud feedback. In contrast, during drier months with lower precipitable water, this feedback mechanism is largely suppressed.

Interestingly, although the mean precipitable water in September is comparable to that in June, July and August, surface cooling is insignificant. This discrepancy is mainly attributed to the weaker

Eurasian warming in September. In response to the rise in CO_2 concentration alone, the surface warming over Eurasia diminishes markedly in September compared with earlier summer months (Supplementary Fig. 3), leading to reduced thermal contrast and weaker upward motion over India. Consequently, the ascent-precipitation feedback and associated cloud enhancement become less effective.

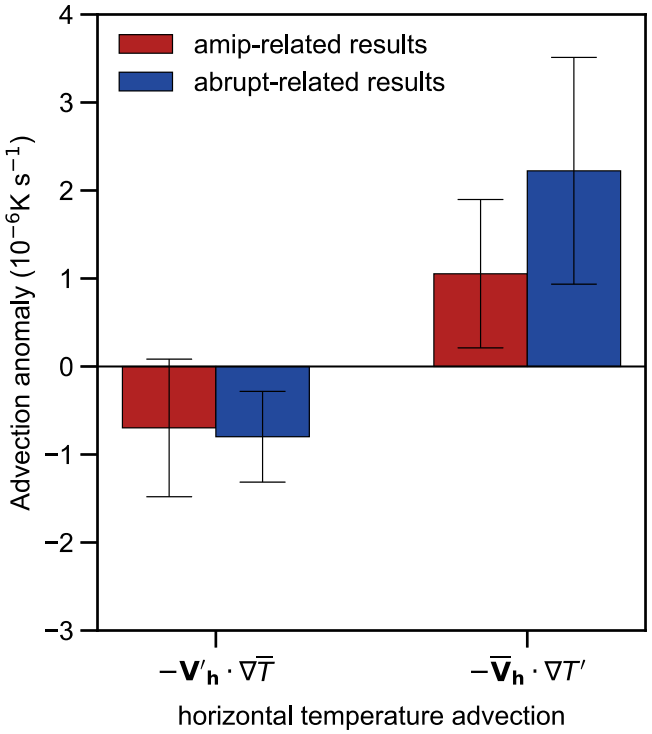

Fig. 5 | Decomposition of near-surface horizontal temperature advection over India. Area average of climatological temperature transported by anomalous horizontal wind ($-\mathbf{V}_{\mathbf{h}}' \cdot \nabla\overline{T}$) and the anomalous temperature transported by climatological horizontal wind ($-\overline{\mathbf{V}_{\mathbf{h}}} \cdot \nabla T'$) based on two kinds of simulations. The red and blue bars indicate the amip-related and abrupt-related results, respectively. Error bars denote the 95% confidence intervals of the multi-model ensemble (MME). These are calculated based on $\pm 1.96 \times \sigma/\sqrt{N}$, where σ denotes the standard deviation across the models, and N is the number of models. The unit is 10^{-6} K s^{-1}.

Therefore, the combined influence of abundant atmospheric moisture and strong Eurasian warming during early summer primarily explains the seasonally confined nature of the CO_2-induced surface cooling over India.

Absence of cooling over East Asia

Unlike India, East Asia—also a monsoon-dominated region with abundant summer moisture[33]—does not exhibit CO_2-induced surface cooling. This contrast highlights the critical role of regional topography and circulation responses in shaping the thermal effect of greenhouse gas forcing.

Despite comparable levels of summer moisture between East Asia and India (Fig. 4c, f), the response of cloud cover diverges sharply. Under increased CO_2 concentration alone, cloud cover decreases over East Asia, preventing the reduction of downward solar radiation that drives surface cooling over India. This suggests that moisture availability alone cannot explain the regional contrast in temperature response.

Topography emerges as a key factor. The Himalayas and the Hindu Kush Mountains, situated north of the Indian subcontinent, act as a barrier that enhances low-level moisture convergence when southwesterly winds intensify under CO_2 forcing. This convergence promotes ascent and increased cloudiness over India. In contrast, East Asia lacks such an orographic barrier along the path of anomalous surface winds (Fig. 4b, e), resulting in weaker moisture convergence and limited cloud formation.

Surface wind patterns further contribute to the contrasting temperature responses. Over India, the anomalous southwesterly winds associated with elevated CO_2 transport relatively cooler air from the Arabian Sea inland, producing cold advection and reinforcing surface cooling (Fig. 4b, e). Such cold advection is absent over East Asia, where the prevailing wind anomalies do not cross strong temperature gradients.

Together, these results indicate that the distinct topographic configuration of the Himalayas–Hindu Kush region, coupled with differential surface wind responses, underpins the absence of CO_2-induced cooling over East Asia. This comparison underscores how regional circulation and terrain jointly modulate the local manifestation of global radiative forcing.

Discussion

The present study reveals a counterintuitive regional cooling over India during boreal summer, directly induced by CO_2 radiative forcing

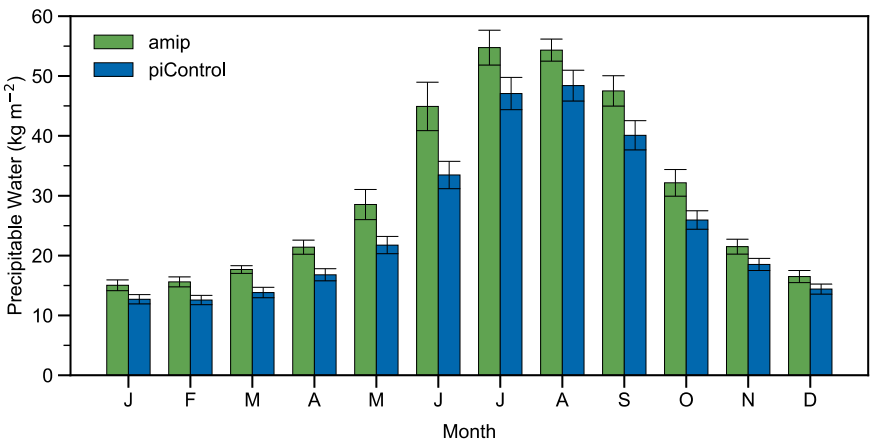

Fig. 6 | Climatology of monthly precipitable water over India. Area-averaged precipitable water over the Indian domain [15–28 °N, 72–87 °E] for each calendar month. Climatology corresponds to 1979–2008 for AMIP (not amip-4 × CO_2) and to the last 30 years for piControl simulations. Green and blue bars indicate the results of amip and piControl simulations, respectively. Error bars denote the 95% confidence intervals of the multi-model ensemble (MME). These are calculated based on $\pm 1.96 \times \sigma/\sqrt{N}$, where σ denotes the standard deviation across the models, and N is the number of models. The unit is kg m^{-2}.

alone, without the influence of oceanic processes or aerosols. This robust signal is consistently identified across two independent CMIP6 experiment frameworks—amip-type simulations with prescribed sea surface temperatures and fully coupled abrupt-4 × CO_2 and piControl simulations. In both cases, a quadrupling of CO_2 concentration leads to pronounced surface cooling over the Indian Peninsula, south of the Himalayas, amid widespread global land warming. This cooling, exceeding 0.1 K since 1950 or earlier, is confined to the lower atmosphere (below 850 hPa) and exhibits strong seasonality, occurring predominantly from June to August.

Mechanistically, the CO_2-induced cooling arises from a cascade of atmospheric adjustments that are triggered by direct radiative forcing. The dominant contributor is a marked reduction in downward solar radiation at the surface, caused by enhanced cloud cover. This increase in cloudiness results from strengthened atmospheric ascent and intensified moisture transport, both amplified under CO_2 perturbation. The rapid warming of the Eurasian continent relative to surrounding oceans enhances the land–sea thermal contrast, reinforcing low-level convergence and upward motion over India. The abundant monsoonal moisture further sustains a positive feedback loop, where enhanced ascent promotes increased cloud formation and precipitation, thereby reducing solar heating at the surface.

In addition, horizontal temperature advection contributes to the near-surface cooling. The anomalous southwesterly winds induced by the rise in CO_2 concentration transport relatively cooler air from the Arabian Sea to India, generating a cold advection effect that amplifies the local temperature decline.

A comparison with East Asia—another monsoon-dominated region that does not exhibit similar cooling—highlights the pivotal role of topography in modulating regional climate responses. The Himalayas and the Hindu Kush Mountains act as an orographic barrier that enhances moisture convergence and ascent over India, a dynamic effect absent in East Asia, where no such barrier constrains the wind anomalies[34,35]. Consequently, while both regions share abundant summer moisture, only India experiences the dynamically enhanced cloud–radiation feedback that yields surface cooling. Together, these findings demonstrate that greenhouse gas forcing can induce localized cooling through a combination of radiatively driven cloud feedbacks and dynamically mediated circulation changes.

These results carry several broader implications for understanding and projecting regional climate responses to greenhouse gas forcing.

(1) Magnitude of climate feedbacks. The cooling effect directly driven by CO_2 radiative forcing may partially offset the warming effects of climate feedbacks over India. Consequently, analyses based on observed summer temperature trends in this region may underestimate the full strength of climate feedback–related warming.

(2) Future CO_2 mitigation scenarios. The projected decline in CO_2 concentration aimed at curbing global warming may, counterintuitively, contribute to warming over India. As our results demonstrate that increased CO_2 forcing induces summer cooling, reduced CO_2 would thus diminish this cooling effect. Consequently, the net regional temperature decrease may be smaller than conventionally anticipated.

(3) Transient response to abrupt forcing. An abrupt increase in CO_2 concentration can temporarily alter the seasonal temperature response over India. In the abrupt-4 × CO_2 simulation, both the first-year and multi-year mean results show that the summer temperature increase is weaker than in other seasons, with a greater proportion of models exhibiting actual cooling during the summer months (Fig. 7a, c). Such behavior is not evident in most other monsoon regions (Supplementary Fig. 6). The ratio of models showing a cooling response is highest over India, both in the first year and in the five-year mean results (Fig. 7b, d), underscoring the robustness of this regional anomaly. In addition, the abrupt-2 × CO_2 simulation exhibits behavior consistent with that in the abrupt-4 × CO_2 simulation, with India showing a local summer cooling anomaly relative to other land monsoon regions (Supplementary Figs. 7, 8). In the abrupt-0.5 × CO_2 simulation, India exhibits a corresponding summer warming anomaly (Supplementary Figs. 9, 10). Overall, these results indicate that the distinct summer temperature responses over India are consistent across different abrupt CO_2 forcing magnitudes.

Collectively, this analysis identifies a previously unrecognized mechanism through which greenhouse gas forcing alone can induce regional surface cooling via atmospheric dynamical and radiative interactions. The results highlight the complexity of regional climate responses to global forcing and underscore the necessity of accounting for such nonlinear processes in projections of future climate change over South Asia.

Methods

CMIP6 dataset

This study employs multiple CMIP6 experiments to evaluate the atmospheric response to direct CO_2 radiative forcing. Specifically, seven types of simulations are analyzed (Detailed model information is provided in Supplementary Table 1):

(1) preindustrial control (piControl): CO_2 concentration is fixed at 284.7 ppm, with a minimum integration length of 500 years[36].
(2) abrupt 4 × CO_2: CO_2 concentration is instantaneously quadrupled relative to the preindustrial level and then held constant for at least 150 simulation years[36].
(3) abrupt 2 × CO_2: CO_2 concentration is instantaneously doubled relative to the preindustrial level and then held constant for at least 150 simulation years[37].
(4) abrupt 0.5 × CO_2: CO_2 concentration is instantaneously halved relative to the preindustrial level and then held constant for at least 150 simulation years[37].
(5) amip: Atmosphere-only simulations forced by observed sea surface temperatures and sea ice concentration for 1979–2014[37].
(6) amip-4 × CO_2 simulation: same SST and sea ice as amip, but with quadrupled CO_2 concentration[37].
(7) historical simulation: Simulations forced by observed natural and anthropogenic drivers from 1850–2014[36].

All model outputs are regridded to a uniform 1° × 1° resolution using bilinear interpolation to construct the MME[38]. A response is considered robust when at least 75% of models agree on the sign of the MME. Some variables are not available, and details of the missing variables are provided in Supplementary Table 2.

To assess model fidelity, simulated surface air temperatures over India are evaluated against the Climatic Research Unit (CRU) v4.09 dataset[39]. The dataset is bilinearly interpolated to a 1° × 1° horizontal resolution. The comparison uses June–August climatology for 1979–2014. Both amip and historical simulations reproduce the observed south–north and west–east temperature gradients across the Indian subcontinent (Supplementary Fig. 4a–c).

Quantitatively, Taylor diagram analysis (Supplementary Fig. 5) shows high spatial correlations with CRU observations. Over [15–28 °N, 72–87 °E], the spatial correlation coefficients of the amip simulation with CRU are 0.68–0.93 (the average is 0.90); the coefficients of the historical simulation are 0.56–0.98 (the average is 0.86). Most models display a reasonably centered root-mean-square error with CRU. These metrics indicate that the selected CMIP6 models reliably capture the observed Indian surface air temperature distribution, providing a robust basis for subsequent analysis.

CRU observational data

The CRU TS (Climatic Research Unit Time Series) dataset provides a high-resolution, long-term global land climate record, with monthly mean surface air temperature available on a 0.5° × 0.5° grid. The

https://doi.org/10.1038/s41467-026-69875-2

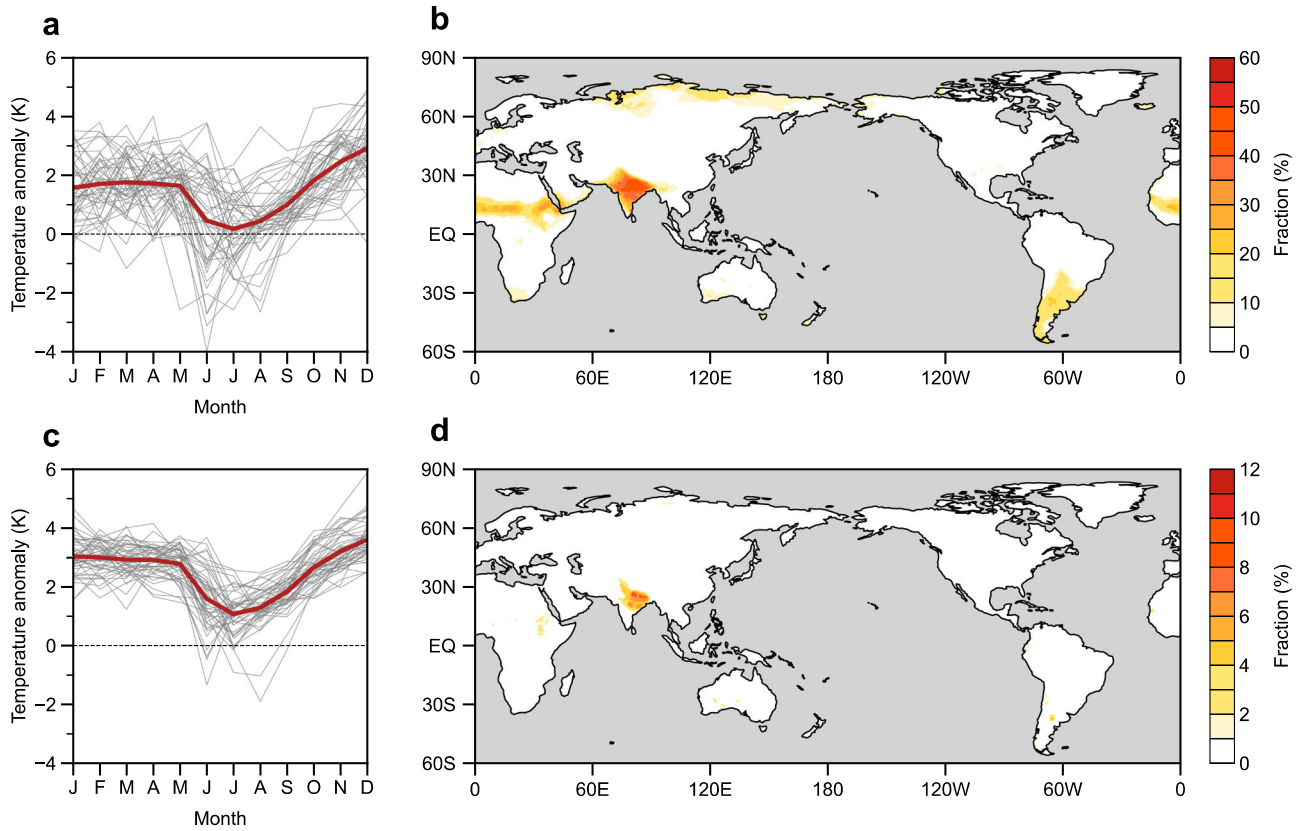

Fig. 7 | Summer cooling response over the Indian surface to increased CO_2 concentration alone. a Monthly surface air temperature response over the Indian domain [15–28 °N, 72–87 °E] during the 1st year after CO_2 is quadrupled. Red line denotes the multi-model ensemble (MME) results, and gray lines represent individual model responses. The unit is K. **b** Fraction of models exhibiting summer cooling in the 1st-year response. The unit is %. **c**, **d** Same as (**a**, **b**), but for the 1–5 year mean after CO_2 is quadrupled. The climate response is evaluated as the difference between the 1st-year or 1–5 year mean of the abrupt-4 × CO_2 simulation and the last 100-year climatology in the piControl simulation.

dataset integrates observations from the World Meteorological Organization (WMO) CLIMAT reports and NOAA's Monthly Climatic Data for the World summaries, following strict quality control procedures.

Version 4 of the dataset spans 1901–2018 and employs an angular-distance weighting interpolation method, enhancing spatial accuracy and traceability between gridded values and station observations. This ensures the dataset's suitability for benchmarking model performance in regional climate analyses.

The global precipitation climatology project

To obtain the domain of land monsoon, this study utilizes the globally complete, monthly Global Precipitation Climatology Project dataset[40], which provides surface precipitation estimates at a spatial resolution of 2.5° latitude × 2.5° longitude from January 1979 onward. The dataset is generated through a merged multi-source approach, integrating low-orbit satellite microwave retrievals, geosynchronous-orbit satellite infrared observations, and surface rain gauge measurements. To optimize accuracy and temporal coverage, the integration strategy employs higher-accuracy microwave data to calibrate the more frequent infrared observations. For the pre-microwave period (prior to mid-1987), the record is extended using infrared-only data adjusted via a calibration derived from later microwave-based analyses. The final satellite-gauge blended product is further corrected using ground-based rain gauge analyses. The archived dataset also includes individual input fields, a merged satellite-only estimate, and associated uncertainty estimates for each variable. This monthly analysis serves as the foundation for the broader suite of GPCP products, including those with higher temporal resolution. In this work, we characterize the 30-year GPCP climatology (1979–2008) and examine its temporal and spatial variability in global precipitation.

Quantification of CO_2 radiative forcing effects

To isolate the direct atmospheric response to CO_2 radiative forcing, two complementary simulation frameworks are used:

(1) The amip-related simulations. In this kind of simulations[41–43], the atmospheric response is estimated from the 30-year climatological difference (1979–2008) between amip-4 × CO_2 and amip simulations. This configuration excludes oceanic feedbacks, allowing a clean diagnosis of atmosphere–land adjustments to increased CO_2.

(2) The abrupt-related simulations. In fully coupled models, global-mean SST variations are regressed out to separate CO_2-driven radiative effects from ocean-mediated changes. Specifically, changes in climate variables are regressed against the global-mean SST changes, and the CO_2-induced response is quantified as the regression intercept at zero global-mean SST anomaly[44,45]. Here, the changes are defined as the difference between the first 150 years in abrupt-4 × CO_2 simulations and the last 100-year climatology in piControl simulations.

Results derived from these two approaches are referred to as "amip-related results" and "abrupt-related results", respectively. Together, these two approaches serve complementary purposes. The amip-related simulations provide a physically clean estimate of the atmospheric–land adjustments by explicitly excluding SST-mediated feedbacks, whereas the abrupt-related simulations allow the CO_2-induced response to be evaluated across a much larger set of models,

thereby improving the robustness and physical consistency of the results.

Thermodynamic framework for near-surface air temperature at 2 m

The anomalous thermodynamic energy equation is expressed as[46]:

$$\partial T'/\partial t = -\mathbf{V_h}' \cdot \nabla \bar{T} - \overline{\mathbf{V_h}} \cdot \nabla T' - \mathbf{V_h}' \cdot \nabla T' - \omega'(\gamma_d - \bar{\gamma}) - \bar{\omega}(\gamma_d - \gamma') - \omega'(\gamma_d - \gamma') + dQ'/\left(C_p dt\right) \quad (1)$$

where T is temperature, $\boldsymbol{V_h}$ denotes the near-surface wind vector, ω represents pressure velocity, γ_d is the dry adiabatic lapse rate, γ is the environmental lapse rate, C_p is the specific heat at constant pressure, and Q denotes the diabatic heating. For variable X, $\bar{X}$ and X' mean the climatology and anomaly, respectively.

On climate-change timescales, the tendencies and nonlinear advection terms are negligible:

$$\partial T'/\partial t \approx 0 \quad (2)$$

$$\mathbf{V_h}' \cdot \nabla T' \approx 0 \quad (3)$$

Near the surface, vertical motions are weak ($\omega \approx 0$), so the vertical adiabatic terms are also negligible. The equation thus simplifies to:

$$-\mathbf{V_h}' \cdot \nabla \bar{T} - \overline{\mathbf{V_h}} \cdot \nabla T' + dQ'/\left(C_p dt\right) \approx 0 \quad (4)$$

Here, the first term represents horizontal temperature advection, and the last term denotes diabatic heating anomalies, which are dominated by radiative and latent heating effects. Although the diabatic term is difficult to evaluate directly, this formulation provides a conceptual basis for decomposing surface temperature responses into advective and radiative components under increased CO_2 forcing.

Definition of the global land monsoon region

The global monsoon region is defined as the area where the local "summer minus winter" precipitation rate exceeds 2.0 mm day^{-1} and where local summer precipitation exceeds 55% of the annual total[47]. Here, local summer is defined as May–September in the Northern Hemisphere and November–March in the Southern Hemisphere. In this study, the global monsoon region is identified based on the climatological precipitation (1979–2008) from the Global Precipitation Climatology Project[40], and only land monsoon regions are considered (Supplementary Fig. 11). The precipitation dataset is bilinearly interpolated to a 1° × 1° horizontal resolution.

Data availability

The CMIP6 outputs are available online at https://esgf-node.llnl.gov/projects/cmip6/. The CRU TS v4.09 surface air temperature dataset is available online at https://crudata.uea.ac.uk/cru/data/hrg/cru_ts_4.09/cruts.2503051245.v4.09/tmp/. The Global Precipitation Climatology Project's monthly precipitation is available online at https://psl.noaa.gov/data/gridded/data.gpcp.html.

Code availability

The source codes used to produce these main results are available from https://zenodo.org/records/18491957. The data in this study were analyzed with the Python programming language.

References

1. IPCC. *Climate Change 2021: The Physical Science Basis. Contribution of Working Group I to the Sixth Assessment Report of the Intergovernmental Panel on Climate Change* (ed. Masson-Delmotte, V. et al.). 2391 (Cambridge, United Kingdom and New York, NY, USA, 2021).
2. Cannon, A. J. Twelve months at 1.5øC signals earlier than expected breach of Paris Agreement threshold. *Nat. Clim. Change* **15**, 266–269 (2025).
3. Forster, P. M. et al. Indicators of Global Climate Change 2024: annual update of key indicators of the state of the climate system and human influence. *Earth Syst. Sci. Data* **17**, 2641–2680 (2025).
4. Eyring, V. et al. Human influence on the climate system: contribution of working group i to the sixth assessment report of the intergovernmental panel on climate change (2021).
5. Xie, S. P. et al. Global warming pattern formation: sea surface temperature and rainfall. *J. Clim.* **23**, 966–986 (2010).
6. Parmesan, C. et al. in *Climate Change 2022: Impacts, Adaptation, and Vulnerability*. (eds Pörtner, H.-O. et al.) 197–377 (Cambridge University Press, 2022).
7. Cissé, G. et al. in *Climate Change 2022: Impacts, Adaptation, and Vulnerability*. (eds Pörtner, H.-O. et al.) 1041–1170 (Cambridge University Press, 2022).
8. Keil, P. et al. Multiple drivers of the North Atlantic warming hole. *Nat. Clim. Change* **10**, 667–671 (2020).
9. Hu, S. N. & Fedorov, A. V. Indian Ocean warming as a driver of the North Atlantic warming hole. *Nat. Commun.* **11**, 4785 (2020).
10. Meehl, G. A., Arblaster, J. M. & Branstator, G. Mechanisms contributing to the warming hole and the consequent us east-west differential of heat extremes. *J. Clim.* **25**, 6394–6408 (2012).
11. Li, K. Y. & Liu, W. Weakened Atlantic Meridional Overturning Circulation causes the historical North Atlantic Warming Hole. *Commun. Earth Environ.* https://doi.org/10.1038/s43247-025-02403-0 (2025).
12. Ferster, B. S., Simon, A., Fedorov, A., Mignot, J. & Guilyardi, E. Slowdown and recovery of the Atlantic meridional overturning circulation and a persistent North Atlantic Warming hole induced by Arctic Sea Ice Decline. *Geophys. Res. Lett.* https://doi.org/10.1029/2022GL097967 (2022).
13. Drijfhout, S., van Oldenborgh, G. J. & Cimatoribus, A. Is a decline of AMOC causing the warming hole above the North Atlantic in observed and modeled warming patterns? *J. Clim.* **25**, 8373–8379 (2012).
14. Fiedler, S. & Putrasahan, D. How does the North Atlantic SST pattern respond to anthropogenic aerosols in the 1970s and 2000s? *Geophys. Res. Lett.* https://doi.org/10.1029/2020GL092142 (2021).
15. Li, Q. X., Luo, Y. Y., Lu, J., Liu, F. K. & Teng, H. L. Roles of the atmosphere and ocean in the projected North Atlantic warming hole. *Clim. Dyn.* **62**, 7465–7480 (2024).
16. Fan, Y. F., Liu, W., Zhang, P. F., Chen, R. & Li, L. F. North Atlantic Oscillation contributes to the subpolar North Atlantic cooling in the past century. *Clim. Dyn.* **61**, 5199–5215 (2023).
17. Eischeid, J. K. et al. Why has the summertime central US warming hole not disappeared? *J. Clim.* **36**, 7319–7336 (2023).
18. Partridge, T. F. et al. Spatially distinct seasonal patterns and forcings of the US warming hole. *Geophys. Res. Lett.* **45**, 2055–2063 (2018).
19. Meehl, G. A., Arblaster, J. M. & Chung, C. T. Y. Disappearance of the southeast US "warming hole" with the late 1990s transition of the Interdecadal Pacific Oscillation. *Geophys. Res. Lett.* **42**, 5564–5570 (2015).
20. Chalif, J. I., Osterberg, E. C. & Partridge, T. F. A wavier polar jet stream contributed to the mid-20th century winter warming hole in the United States. *Agu Advances* https://doi.org/10.1029/2024AV001399 (2025).
21. Mascioli, N. R., Previdi, M., Fiore, A. M. & Ting, M. F. Timing and seasonality of the United States `warming hole'. *Environ. Res. Lett.* 12, 034008 (2017).

22. Chandrashekhar, V. A global warming 'hole' where you'd least expect it. *Science* **388**, 136–136 (2025).
23. Dodla, V. B., Satyanarayana, G. C. & Desamsetti, S. Analysis and prediction of a catastrophic Indian coastal heat wave of 2015. *Nat. Hazards* **87**, 395–414 (2017).
24. ul Hassan, W. et al. Unveiling the devastating effect of the spring 2022 mega-heatwave on the South Asian snowpack. *Commun. Earth Environ.* https://doi.org/10.1038/s43247-024-01857-y (2024).
25. Singh, H., Dube, A., Ashrit, R., Srivastava, P. K. & Prasad, V. S. Object-based forecasting of heat waves over India: a novel approach. *J. Earth Syst. Sci.* https://doi.org/10.1007/s12040-025-02584-4 (2025).
26. Marathe, S. et al. North Atlantic fingerprint on severe heatwaves over the Indian region. *Q. J. R. Meteorol. Soc.* https://doi.org/10.1002/qj.70061 (2025).
27. Rohini, P., Rajeevan, M. & Srivastava, A. K. On the variability and increasing trends of heat waves over India. *Sci. Rep.* **6**, 26153 (2016).
28. Panda, D. K., Pradhan, S. & AghaKouchak, A. Surface drying impacts hot extremes in India: unravelling the exceptional 2010 and 2016 hot events. *Clim. Dyn.* **60**, 3785–3800 (2023).
29. Lan, X., Tans, P. & Thoning, K. W. *Trends in globally-averaged CO2 determined from NOAA Global Monitoring Laboratory measurements*. Global Monitoring Laboratory https://gml.noaa.gov/ccgg/trends/global.html (2025).
30. Rubino, M. et al. *Law Dome Ice Core 2000-Year CO2, CH4, N2O and d13C-CO_2*. CSIRO Data Collection https://doi.org/10.25919/5bfe29ff807fb (2019).
31. Held, I. M. & Soden, B. J. Robust responses of the hydrological cycle to global warming. *J. Clim.* **19**, 5686–5699 (2006).
32. Li, X. Q. & Ting, M. F. Understanding the Asian summer monsoon response to greenhouse warming: the relative roles of direct radiative forcing and sea surface temperature change. *Clim. Dyn.* **49**, 2863–2880 (2017).
33. Liu, F. et al. Opportunities and barriers for skillful subseasonal prediction of East Asian summer precipitation. *Bull. Am. Meteorol. Soc.* **105**, E2216–E2230 (2024).
34. Boos, W. R. & Kuang, Z. Dominant control of the South Asian monsoon by orographic insulation versus plateau heating. *Nature* **463**, 218–222 (2010).
35. Wu, G. et al. Thermal controls on the Asian summer monsoon. *Sci. Rep.* **2**, 404 (2012).
36. Eyring, V. et al. Overview of the Coupled Model Intercomparison Project Phase 6 (CMIP6) experimental design and organization. *Geosci. Model Dev.* **9**, 1937–1958 (2016).
37. Webb, M. J. et al. The Cloud Feedback Model Intercomparison Project (CFMIP) contribution to CMIP6. *Geosci. Model Dev.* **10**, 359–384 (2017).
38. Press, W. H., Teukolsky, S. A., Vetterling, W. T. & Flannery, B. P. *Numerical recipes 3rd edition: The art of scientific computing*. 110–150 (Cambridge, United Kingdom and New York, NY, USA, 2007).
39. Harris, I., Osborn, T. J., Jones, P. & Lister, D. Version 4 of the CRU TS monthly high-resolution gridded multivariate climate dataset. *Scientific Data* https://doi.org/10.1038/s41597-020-0453-3 (2020).
40. Adler, R. F. et al. The version-2 global precipitation climatology project (GPCP) monthly precipitation analysis (1979-present). *J. Hydrometeorol.* **4**, 1147–1167 (2003).
41. Chadwick, R., Ackerley, D., Ogura, T. & Dommenget, D. Separating the influences of land warming, the direct CO_2 effect, the plant physiological effect, and SST warming on regional precipitation changes. *J. Geophys. Res.-Atmos.* **124**, 624–640 (2019).
42. Shaw, T. A. & Voigt, A. Tug of war on summertime circulation between radiative forcing and sea surface warming. *Nat. Geosci.* **8**, 560–U105 (2015).
43. Chadwick, R. Which aspects of CO2 forcing and SST warming cause most uncertainty in projections of tropical rainfall change over land and Ocean? *J. Clim.* **29**, 2493–2509 (2016).
44. Sherwood, S. C. et al. Adjustments in the forcing-feedback framework for understanding climate change. *Bull. Am. Meteorol. Soc.* **96**, 217–228 (2015).
45. Gregory, J. M. et al. A new method for diagnosing radiative forcing and climate sensitivity. *Geophys. Res. Lett.* **31**, L03205 (2004).
46. Holton, J. R. & Hakim, G. J. *An introduction to dynamic meteorology* 56–57 (Academic Press, MA, USA, 2013).
47. Wang, B. & Ding, Q. H. Global monsoon: Dominant mode of annual variation in the tropics. *Dyn. Atmos. Oceans* **44**, 165–183 (2008).

Acknowledgments

We acknowledge the World Climate Research Program, which, through its Working Group on Coupled Modeling, coordinated and promoted CMIP6. We thank the climate modeling groups for producing and making available their model output, the Earth System Grid Federation (ESGF) for archiving the data and providing access, and the multiple funding agencies that support CMIP6 and ESGF. The study was supported by the National Natural Science Foundation of China (42530606, X.Q. and 42261144687, G.H.).

Author contributions

X.Q. and G.H. conceived the study; J.H.L. performed the analysis; J.H.L. and X.Q. wrote and revised the paper; G.H. revised the paper. J.H.L., X.Q., and G.H. discussed and commented on the paper. C.L.L. prepared the simulation data.

Competing interests

The authors declare no competing interests.

Additional information

Supplementary information The online version contains supplementary material available at https://doi.org/10.1038/s41467-026-69875-2.

Correspondence and requests for materials should be addressed to Xia Qu or Gang Huang.

Peer review information *Nature Communications* thanks Popat Salunke and the other anonymous reviewer for their contribution to the peer review of this work. A peer review file is available.